remote sensing

MDPI

Article

Estimating Water Depth of Different Waterbodies Using Deep Learning Super Resolution from HJ-2 Satellite Hyperspectral Images

Shuangyin Zhang [1], Kailong Hu [2], Xinsheng Wang [3,*], Baocheng Zhao [1], Ming Liu [2], Changjun Gu [2], Jian Xu [1] and Xuejun Cheng [1]

[1] Changjiang River Scientific Research Institute, Changjiang Water Resources Committee, Wuhan 430010, China
[2] Key Laboratory of Emergency Satellite Engineering and Application, Ministry of Emergency Management, Beijing 100024, China
[3] State Key Laboratory of Information Engineering in Surveying, Mapping, and Remote Sensing, Wuhan University, Wuhan 430079, China
* Correspondence: wangxsh8@whu.edu.cn

Abstract: Hyperspectral remote sensing images offer a unique opportunity to quickly monitor water depth, but how to utilize the enriched spectral information and improve its spatial resolution remains a challenge. We proposed a water depth estimation framework to improve spatial resolution using deep learning and four inversion methods and verified the effectiveness of different super resolution and inversion methods in three waterbodies based on HJ-2 hyperspectral images. Results indicated that it was feasible to use HJ-2 hyperspectral images with a higher spatial resolution via super resolution methods to estimate water depth. Deep learning improves the spatial resolution of hyperspectral images from 48 m to 24 m and shows less information loss with peak signal-to-noise ratio (PSNR), structural similarity (SSIM), and spectral angle mapper (SAM) values of approximately 37, 0.92, and 2.42, respectively. Among four inversion methods, the multilayer perceptron demonstrates superior performance for the water reservoir, achieving the mean absolute error (MAE) and the mean absolute percentage error (MAPE) of 1.292 m and 22.188%, respectively. For two rivers, the random forest model proves to be the best model, with an MAE of 0.750 m and an MAPE of 10.806%. The proposed method can be used for water depth estimation of different water bodies and can improve the spatial resolution of water depth mapping, providing refined technical support for water environment management and protection.

Keywords: water depth; super resolution; hyperspectral; deep learning; HJ-2A/B

check for updates

Citation: Zhang, S.; Hu, K.; Wang, X.; Zhao, B.; Liu, M.; Gu, C.; Xu, J.; Cheng, X. Estimating Water Depth of Different Waterbodies Using Deep Learning Super Resolution from HJ-2 Satellite Hyperspectral Images. *Remote Sens.* **2024**, *16*, 4607. https://doi.org/10.3390/rs16234607

Academic Editors: Xi Chen, Mingqiang Guo and Antonios Emmanouil Chatzipavlis

Received: 5 November 2024
Revised: 28 November 2024
Accepted: 6 December 2024
Published: 8 December 2024

Copyright: © 2024 by the authors. Licensee MDPI, Basel, Switzerland. This article is an open access article distributed under the terms and conditions of the Creative Commons Attribution (CC BY) license (https://creativecommons.org/licenses/by/4.0/).

1. Introduction

Water depth is crucial for the conservation and management of reservoirs, rivers, and oceans, providing crucial information on underwater topography and sediment loads [1,2]. Various techniques have been applied to measure water depth, including echosounder approaches, aerial LiDAR, and remote sensing [3–5]. Echosounders are highly weather-dependent, while LiDAR is costly [6,7]. Optical remote sensing offers a solution for rapid, large-scale water depth measurements [3], and multispectral images (MSIs) have been widely employed for this purpose [8–10]. These study areas include lakes (e.g., Lake Naivasha [11] and Dongting Lake [9]), rivers [12], and coastal waters [13,14], using MSIs from satellites like Landsat, Sentinel-2 and GF-1 [2,8,9,15–17].

Accurate water depth estimation remains challenging due to variations in suspended particulate matter, phytoplankton blooms, and colored dissolved organic material [18], which is known to modify the water light environment and attenuation [19]. Especially when extreme events such as droughts and floods occur, these parameters change sharply in a short time, further increasing the difficulty of monitoring water depth using MSI [20].

Recent studies highlight these limitations and underscore the need for more effective methodologies [1]. Satellites with sophisticated hyperspectral sensors present an alternative [21]. Hyperspectral image (HSI) provides enriched spectral information, enhancing water depth estimation in various water bodies [22]. For example, Legleiter and Roberts [12] developed a forward image model to estimate river water depth with an R^2 of 0.71 based on simulated HSI data, illustrating the capability of high spectral resolution in complex water environments. Similarly, Jay and Guillaume [23] demonstrated the effectiveness of HSIs in turbid coastal waters, revealing how nuanced spectral signatures can be used to infer depth-related information even under challenging conditions. However, the generally low spatial resolution of HSI limits its effectiveness for fine-scale water depth mapping.

Recently, deep learning (DL)-based super resolution (SR) methods have been increasingly applied to improve the spatial resolution of satellite-derived water characteristics [24]. Leveraging the strong learning capability of deep learning, scholars have developed novel algorithms to enhance the spatial resolution of HSIs [25–28]. They show encouraging results for water depth retrieval, with the potential to reach less than 30 m resolution obtained by deep learning [17]. On the other hand, many methods for fusing hyperspectral and multispectral images have been developed, offering an effective approach to enhancing the resolution of hyperspectral images [29–32]. However, fusion-based methods rely on multisource data, necessitating the alignment and integration of geometric and radiometric properties across datasets, which imposes significant data constraints. In contrast, SR-based methods require only a single HSI, eliminating the need for multisource data and thus greatly reducing data limitations. This advantage serves as the foundation for this study. Combining these SR methods with advanced hyperspectral satellite imagery could potentially enhance the spatial resolution of HSIs, allowing for more accurate water depth estimations across diverse water bodies. Nevertheless, this feasibility remains underexplored.

On 27 September 2020, the Environmental Disaster Reduction II Satellite (HJ-2) was launched in a two-star configuration (HJ-2A and HJ-2B). Both HJ-2A and HJ-2B satellites are equipped with hyperspectral imagers, capable of providing HSI data at a 48-m resolution. The sensors cover a broad spectral range (450–2500 nm), facilitating detailed analyses of water bodies under various conditions. Preliminary assessments suggest that HJ-2 data can provide reliable estimations of water parameters like water quality (chlorophyll-a) [33], but comprehensive investigations into its reliability in monitoring water depth are still limited.

The primary objective of this study is to investigate the feasibility of using HJ-2 HSI data with enhanced spatial resolution via SR methods for water depth estimation. Specifically, we aim to: (1) analyze the feasibility of using DL-based SR methods to improve the spatial resolution of HJ-2 HSI; (2) evaluate the performance of varying retrieval algorithms for water depth estimation across waterbodies; (3) make a comparison of the retrieval algorithms for water depth estimation.

2. Materials and Methods

2.1. Study Areas

The study area (Figure 1) includes three waterbodies: Shenzhen Reservoir, Changtan-Cili River, and Chalin-Sanjiangkou River. Shenzhen Reservoir (22°56′–22°61′N and 114°13′–114°20′E) is located in northeastern Shenzhen City and serves as the primary drinking water source for both Shenzhen and Hong Kong. It spans over 60 square kilometers, with a capacity exceeding 45 million cubic meters and an average water depth of approximately 30 m. The Changtan-Cili River (29°41′–29°48′N and 111°01′–111°13′E) and Chalin-Sanjiangkou River (29°49′–29°59′N and 111°12′–111°27′E) are sections of the Lishui River, situated in the northwestern Hunan Province. The Lishui River flows southwest to northeast, passing through natural channels and towns before eventually joining Dongting Lake. The Changtan-Cili River ranges from 98 m at its narrowest width to 517 m at its widest, while the Chalin-Sanjiangkou River spans from 130 m at its narrowest to 410 m at its widest. While the water environment in these three study areas is relatively good, the

Changtan-Cili River, which traverses the urban areas, is vulnerable to the impacts of urban development and human activities.

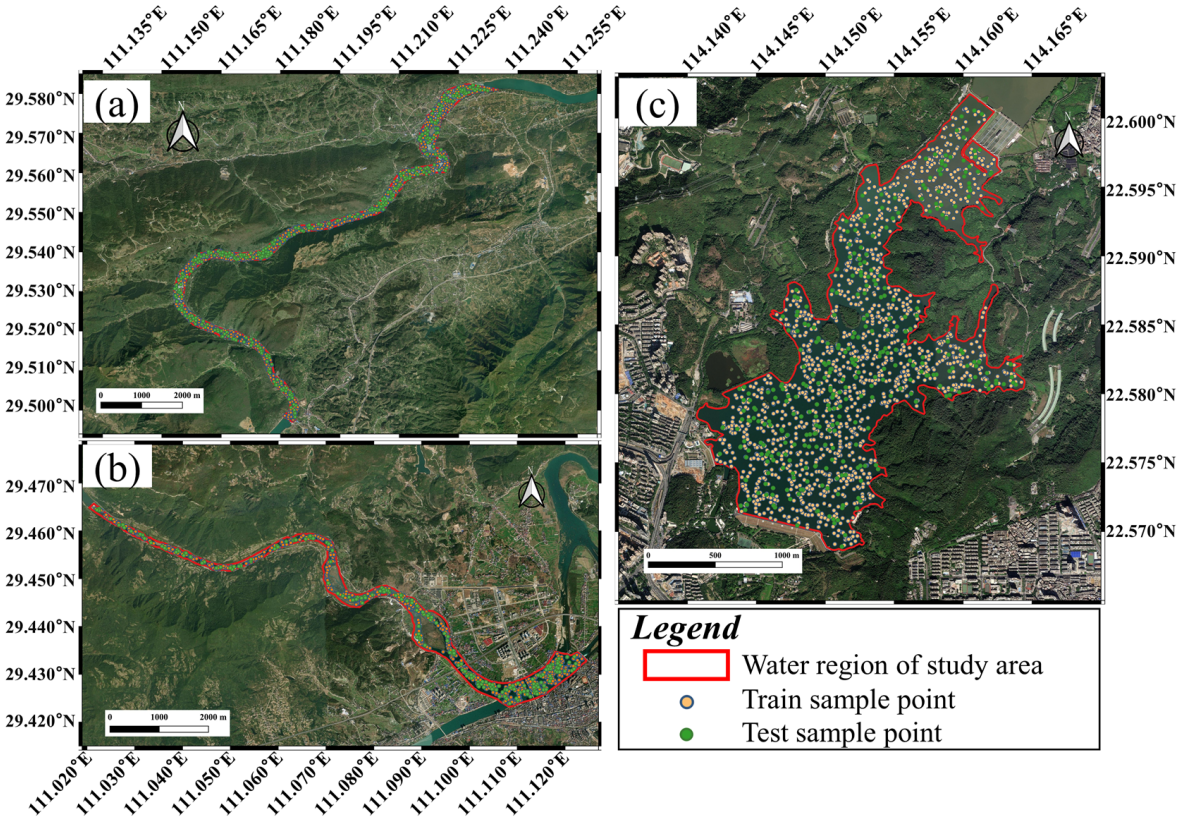


Figure 1. Study areas and distribution of sample points. (**a**) Chalin-Sanjiangkou River; (**b**) Changtan-Cili River; (**c**) Shenzhen Reservoir.

2.2. Satellite Data and Water Depth Data

We collected HSIs of the HJ2-A/B satellite over the designated study areas and obtained real water depth data through field measurements. We selected the visible to near infrared (VNIR) HSIs with a spatial resolution of 48 m, comprising 100 bands covering a wavelength range of 450–920 nm. To investigate the potential of SR technology for water depth inversion using satellite HSIs, we selected thirteen HJ-2A/B satellite HSIs from the Wuhan area for SR model training, considering water scene requirements and geographic differences. Specifically, these images were cut into 620 nonoverlapping patches of 240 × 240 pixels as high resolution (HR) images, while the corresponding low resolution (LR) images were then created by applying bicubic downsampling with a scale factor of 2. Examples of HSI SR datasets and HJ-2 HSIs from the study areas are shown in Figure 2.

An unmanned ship equipped with a HN-400 multibeam sounding system (Shanghai Huace Navigation Technology Ltd., Shanghai, China) was used to measure the water depth. The system operates at a frequency of 200–700 KHz and has an ultra-narrow beam of 0.5° × 1°, with a coverage width from 7° to 210°. The maximum measurable depth is approximately 250 m. The system is capable of transmitting and receiving acoustic waves at a wide angle. As the ship sails along its route, strip-type, high-density water depth data is collected. The unmanned ship with the multibeam system and its measuring results are shown in Figure 3.

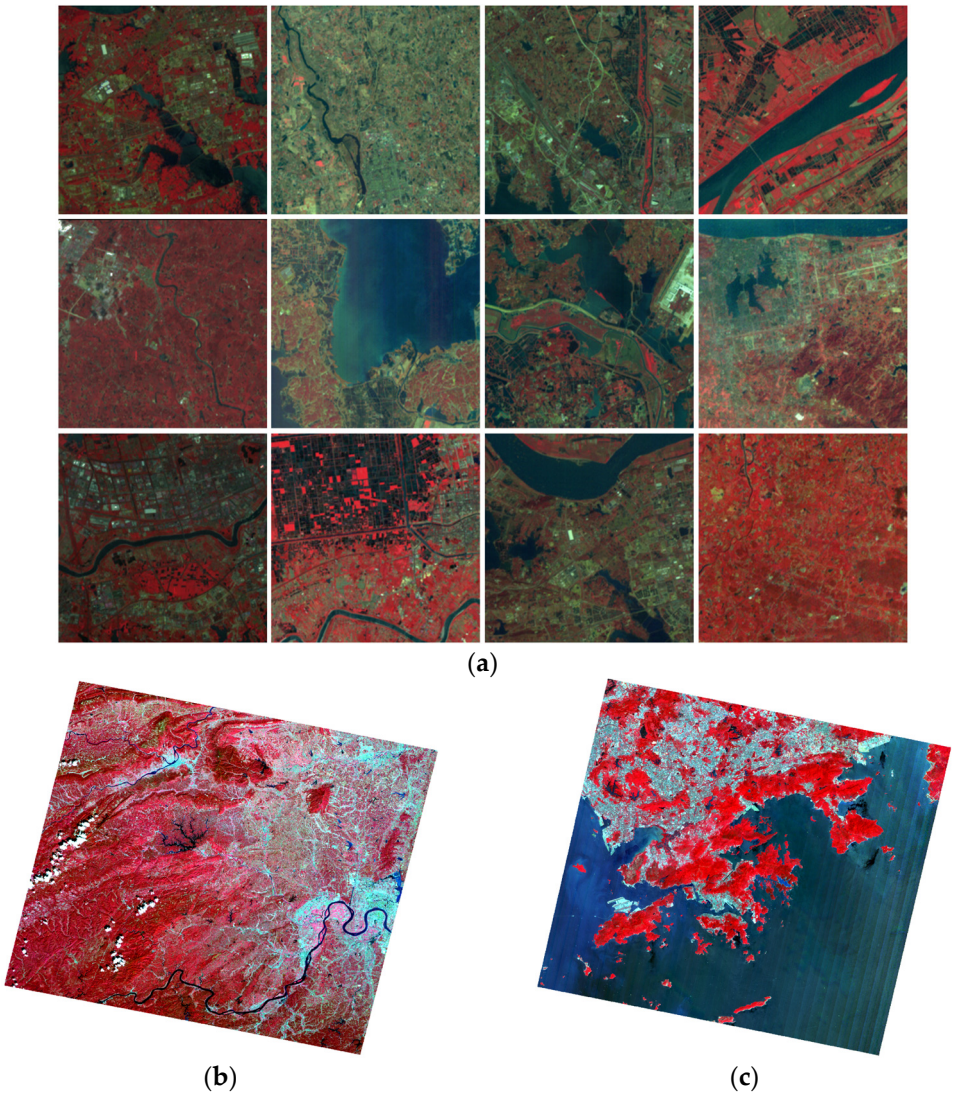


Figure 2. Study data. (**a**) Examples of HJ-2 A/B HSI SR dataset; (**b**) HSI of Chalin-Sanjiangkou River and Changtan-Cili River areas; (**c**) HSI of Shenzhen Reservoir area.



Figure 3. Unmanned ship equipped with multibeam and its measuring results.

2.3. Methods

The flowchart of this study is presented in Figure 4. First, we train multiple HSI SR models using the constructed HJ-2 satellite HSI SR dataset and perform SR processing on the original LR HSIs. Next, a data preprocessing operation is conducted, primarily involving radiometric and geometric corrections. Radiometric preprocessing includes absolute radiometric calibration and atmospheric correction, while geometric preprocessing involves rational polynomial coefficient (RPC) refinement and geometric correction to ensure the spatial alignment between the processed HSI image and the measured water depth data. After preprocessing, a set of sample points is randomly selected based on the measured water depth data and HSIs, and these samples are used to train water depth inversion models. Finally, we validate the accuracy of water depth inversion. To examine the effect of SR on water depth inversion, we apply the above procedure to the original LR images as well.

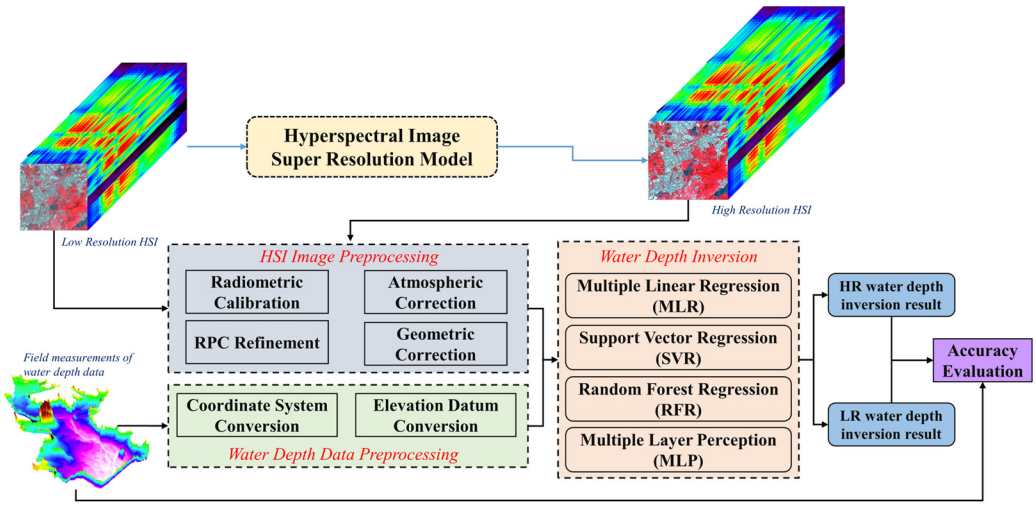


Figure 4. Flow chart of HJ2-AB hyperspectral image water depth inversion.

2.3.1. Deep Learning-Based Hyperspectral Image Super Resolution

- Natural Image Super Resolution
- SRCNN [34] is the first deep learning-based end-to-end network, stacking three convolutional layers to create a lightweight SR model. Building on a generative adversarial network (GAN) [35], SRGAN [36] introduced a new approach to SR tasks. SRGAN comprises a generator and a discriminator that interact in an adversarial mechanism: the generator extracts image features and generates a realistic image, while the discriminator assesses whether the generated image closely resembles a true HR image. The EDSR [37] network, derived from the generator of SRGAN, improves performance by removing batch normalization layers of residual blocks. Unlike SRGAN, ESRGAN [38] enhances the generator further by replacing the original residual blocks with residual-in-residual dense blocks, resulting in higher SR quality. To recover high-frequency details and avoid treating all channels equally, RCAN [39] introduces a channel attention mechanism that adaptively adjusts the channel weights based on deep image features. In contrast, the PAN [40] network enhances SR effects by applying pixel attention. The A^2N [41] network employs a dual branch design to dynamically adjust the weights of the attention module according to the image features, reducing ineffective attention and minimizing model parameters. Additional models [42–44] aim to reduce the computational complexity and memory consumption of SR tasks, further advancing the development and application of SR technology.
- Hyperspectral Image Super Resolution
- Given the significant advancements in SR methods for natural images, some scholars have introduced transfer learning to apply knowledge learned from natural image

SR to HSI SR tasks [45]. In HSI SR research, many methods require the registration of LR-HSI with the corresponding HR multispectral image, which further restricts the application scenarios [46,47]. The GDRRN [48] network is developed for single HSI SR, enabling nonlinear mapping of HSI features through a global residual structure and the grouped recursive module. To address the unique channel dimensions and complex spectral patterns in HSIs, the SSPSR [25] network incorporates spatial-spectral prior to fully utilize spatial information and correlation between hyperspectral spectra. The GELIN [26] approaches HSI SR from a hyperspectral channel perspective, processing data in a group-by-group manner to reduce the computational load of redundant channel information. On the basis of group-wise processing, the RFSR [27] model introduces feedback embedding to construct continuous information between groups, further enhancing HSI SR performance. To leverage the multiscale features of HSIs, the FPNSR [49] model employs a feature pyramid block, demonstrating the effectiveness of multiscale features in HSI SR tasks. Similar to SRGAN, GAN architecture has also been adapted for the HSI SR task [50].

- SR Model Training Details

The experiments were conducted using an NVIDIA RTX 3090 24 GB GPU on the Ubuntu 20.04 operating system with PyTorch 1.12.1 [51]. Each SR model was trained for 100 epochs using the L1 loss function and a batch size of 16. The learning rate was set to 2e−4 initially and dynamically adjusted during training: if the PSNR metric did not increase for 10 epochs, the learning rate would be halved. The training process was optimized by Adam [52] with parameters β_1 = 0.9 and β_2 = 0.999. Input images were normalized to [0, 1] to ensure stable training. Random flipping and transposition were applied solely for data augmentation.

2.3.2. Hyperspectral Image Preprocessing

- Radiometric Preprocessing
- To conduct the subsequent water depth inversion, we must first preprocess the HSI of the HJ-2 A/B satellite, focusing on radiometric and geometric corrections. The pixel values in the original HSI represent the digital number (DN) recorded by the satellite sensor and lack actual physical significance. Consequently, radiometric correction is necessary to convert the DN values into radiance. The radiometric correction formula is as follows:

$$L = K * DN + B \tag{1}$$

where L and DN refer to the radiance value and digital number, respectively. The K and B denote the gain and bias from the radiometric calibration coefficients provided by the satellite image vendors. The radiometric calibration coefficients of the HJ-2 A/B satellite used in this study were obtained from the China Resources Satellite Application Center website (https://www.cresda.cn/zgzywxyyzx/zlxz/article/20240416163618563132683.html accessed on 5 November 2024).

To further obtain the reflectance values, atmospheric correction must be applied following radiometric correction to eliminate the effects of clouds and atmospheric interference on subsequent water depth inversion. In this study, the atmospheric correction is performed using the quick atmospheric correction (QUAC) model in ENVI software.

- Geometric Preprocessing

The positioning accuracy of satellite images is influenced by many factors such as satellite attitude, atmospheric conditions, and imaging devices. To align the HSIs with the actual water depth data collected through field measurement, geometric correction preprocessing is necessary to unify the two images in space dimensions. Given that the spatial resolution of the HSI in the VNIR band of the HJ-2 A/B satellite is approximately 48 m, we selected a higher resolution digital orthophoto image (DOM) at 15 m as a reference to extract ground control points (GCPs). We then performed RPC refinement and geometric

correction based on the methods described in [53,54], ensuring that the positioning accuracy between the processed and reference images is less than one pixel, thus allowing for reliable sample point extraction in subsequent water depth inversion. Additionally, the field-measured water depth data requires preprocessing, including the horizontal projection coordinate system transformation and the elevation datum unification.

2.3.3. Hyperspectral Image Water Depth Inversion

To avoid concentrated distribution of sample points, we utilized QGIS 3.34.2 software to randomly generate sample points in each study area, ensuring that the sample points covered the entire water body as evenly as possible. This approach minimizes the risk of model overfitting due to spatial autocorrelation that can arise from overly clustered sample points [55]. Specifically, for each study area, we randomly extracted certain sample points and divided them into the training and verification set of water depth inversion with the ratio of 8:2. Each sample point contains the corresponding measured water depth value and the reflectance values of 100 bands. Among them, there are 1421 training sample points and 339 test sample points in Shenzhen Reservoir, 807 training sample points and 200 test sample points in Changtan-Cili River and, 1391 training sample points and 343 test samples in Chalin-Sanjiangkou River. Based on these sample points, we selected the following four depth inversion models for training and accuracy verification. The distribution map of selected sample points in three study areas is illustrated in Figure 1. For model selection, we employed multiple linear regression (MLR), random forest (RF), support vector regression (SVR), and multilayer perceptron (MLP) machine learning models to invert water depth. These models have been widely used in previous studies on water depth inversion [56–58], and their well-established algorithms facilitate easy implementation and secondary development. Although there are some DL-based water depth inversion models [59–62], the limited number of sample points in this study led to the exclusive use of machine learning methods for the water depth inversion model.

- MLR

The multiple linear regression model is a simple, yet classical statistical regression model commonly used in straightforward prediction tasks where a linear relationship is plausible. It establishes a linear model between water depth values and reflectance values in different HSI bands:

$$Z = a_0 + a_1x_1 + a_2x_2 + \cdots + a_{100}x_{100} \quad (2)$$

where Z is the water depth value predicted by the model, a_{i} are the coefficients, and x_{i} are the reflectance values for each band.

- RF

The random forest regression model is a supervised learning approach that builds multiple decision trees during training and outputs the average prediction of the individual trees. This approach enhances predictive accuracy and helps avoid overfitting. Random forests are highly versatile and can handle complex, nonlinear relationships while providing measures of feature importance. In terms of RF model parameter setting, the number of trees was set to 800, the squared error was selected as the criterion, and the minimum number of samples required to be at a leaf node was set to 1.

- SVR

Support vector regression is a type of support vector machine (SVM) applied to regression tasks. It finds a hyperplane in a high-dimensional space that best fits the data by optimizing a convex quadratic programming problem, intending to minimize errors within a margin of tolerance. SVR is effective for complex, nonlinear relationships due to the ability to map input features to high-dimensional spaces through its kernel functions, making it suitable for datasets with significant noise or complex patterns. Common kernel functions include linear kernels, polynomial kernels, Gaussian kernels, and radial basis

function (RBF) kernels. When SVR was used for water depth inversion, RBF was selected as the kernel function, the regularization parameter was set to 0.05, and the maximum number of iterations was set to 10,000.

- MLP

A multilayer perceptron is a type of artificial neural network composed of an input layer, one or more hidden layers, and an output layer. Each layer consists of neurons that process inputs through weighted connections. MLPs can model complex, nonlinear relationships, making them well-suited for the water depth inversion task. For the MLP parameter settings, three hidden layers are selected, with the number of each layer being 100, 400, and 20, respectively. The rectified linear unit function (ReLU) was selected as the activation function, and the stochastic gradient descent (SGD) optimizer was employed for optimization. The learning rate was set to 0.001, and the maximum number of iterations was set to 10,000.

2.4. Accuracy Evaluation Metrics

The accuracy evaluation metrics used in this study involve two tasks, among which the metrics of the HSI SR task are peak signal-to-noise ratio (PSNR), structural similarity (SSIM), and spectral angle mapper (SAM), and the metrics of water depth inversion are mean absolute error (MAE) and mean absolute percentage error (MAPE).

2.4.1. Super Resolution Metrics

- PSNR
- PSNR, the most common and widely used metric for evaluating image quality, calculates the ratio of the maximum signal value to the noise intensity. Higher PSNR means better image quality. It is defined as follows:

$$\mathrm{PSNR} = 10 * \log_{10} \frac{Max_I^2}{\frac{1}{N}\sum_{i=1}^{N}\left(I_{GT}(i) - I_{SR}(i)\right)^2} \tag{3}$$

where Max_I^2 refers to the maximum pixel value of the image, I_{GT} and I_{SR} refer to HR image and super-resolved image, respectively. N represents the total number of pixels in the image.

- SSIM
- The SSIM calculates the structural similarity between two images. It is calculated by using the mean values and the standard deviations of images. The greater the SSIM, the closer the structures of the two images are. The definition of SSIM is shown as follows:

$$\mathrm{SSIM} = \frac{(2\mu_{GT}\mu_{SR} + C_1)(2\sigma_{GT}\sigma_{SR} + C_2)}{\left(\mu_{GT}^2 + \mu_{SR}^2 + C_1\right)\left(\sigma_{GT}^2 + \sigma_{SR}^2 + C_1\right)} \tag{4}$$

where μ_{GT} and μ_{SR} represent the mean values of the HR and SR images, the σ_{GT} and σ_{SR} denote the corresponding standard deviations of the HR and SR images, respectively. C_1 and C_2 are two constants to avoid denominators of 0.

- SAM
- SAM considers the spectrum of each pixel in the image as a high-dimensional vector and measures the similarity between the spectra by calculating the angle between the two vectors [63]. The smaller the SAM, the more similar the two spectra, indicating a higher likelihood that they represent the same type of ground object. The SAM is defined as follows:

$$\mathrm{SAM} = \frac{1}{N}\sum_{i=1}^{N}\cos^{-1}\left(\frac{\boldsymbol{Y}_i^T\boldsymbol{X}_i}{\left\|\boldsymbol{Y}_i^T\right\|\|\boldsymbol{X}_i\|}\right) \tag{5}$$

where $\boldsymbol{X_i}$ and $\boldsymbol{Y_i}$ refer to two spectral vectors of the same pixel i from two images. N represents the total number of pixels in the image.

2.4.2. Water Depth Inversion Metrics

- MAE
- MAE directly measures the average difference between two sets of water depth values. It can be calculated as follows:

$$\mathrm{MAE} = \frac{1}{N}\sum_{i=1}^{N}\left|\hat{d}_i - d_i\right| \tag{6}$$

where $\hat{d}_i$ and d_i refer to the predicted water depth value and true water depth value of sample point i, while N represents the total number of sample points used for validation.

- MAPE
- MAPE is sensitive to relative error and does not change due to the global scaling of the target variable, which is suitable for the problem of a large gap in the dimension of the target variable. It is defined as follows:

$$\mathrm{MAPE} = \frac{100\%}{N}\sum_{i=1}^{N}\left|\frac{\hat{d}_i - d_i}{d_i}\right| \tag{7}$$

3. Results and Analysis

3.1. Super Resolution Results

3.1.1. SR Accuracy on HSI SR Dataset

- We first evaluated the accuracy of the selected SR methods on the test set of the HSI SR dataset. As shown in Table 1, the FPNSR method achieves the highest accuracy across all three metrics, followed by the GDRRN method. Compared with the traditional bicubic interpolation method, the deep learning-based SR model shows substantial performance improvements.

Table 1. SR results on the HSI dataset.

Method	PSNR	SSIM	SAM	Parameters	Flops
BICUBIC	35.7769	0.9041	4.7413	/	/
FPNSR	37.0493	0.9226	2.4206	44.132M	1.261T
SSPSR	36.9121	0.9206	2.4476	11.011M	1.092T
GDRRN	36.7055	0.9169	2.5263	0.378M	89.712G

- Additionally, we compared the parameter count and computational load of each DL-based SR network. As shown in Table 1, among the three DL-based SR models, the FPNSR network achieved the best accuracy metrics but required the largest parameters and the highest computation load. Conversely, the GRDDN network had the smallest parameter count and computation load but delivered the lowest accuracy metrics. This highlights a limitation of DL-based SR networks: higher accuracy often comes at the cost of more parameters and increased computational burden and the need for GPU hardware to ensure practical application timeliness. In contrast, the traditional bicubic interpolation method imposes fewer restrictions, does not rely on model training or GPU hardware, and maintains competitive accuracy metrics.

3.1.2. SR Results of Study Areas

The SR models trained on the constructed HSI SR dataset were further applied to HSIs from the study areas. Since no corresponding HR HSIs exist as ground truth, we only compare the qualitative results across different SR methods. As shown in Figure 5, the results of the BICUBIC method exhibit significant blurring effects, particularly along river and bridge boundaries. In contrast, the other three deep learning models show markedly improved visual quality, with the FPNSR network preserving finer details in small ground object structures.

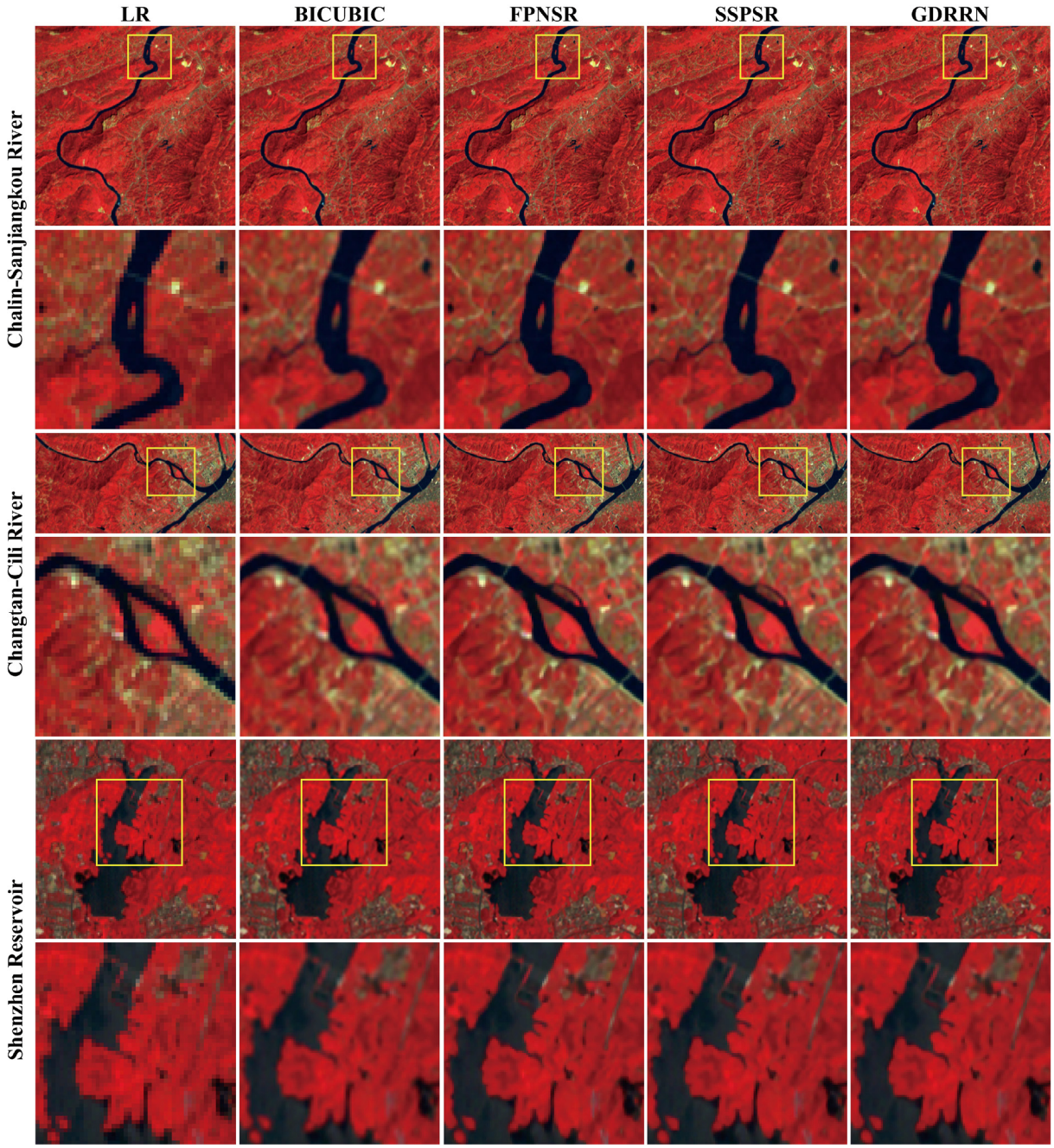


Figure 5. SR results of HJ2-A/B HSI images on the study area (shown in false color combination).

3.2. Water Depth Inversion Results

3.2.1. Water Depth Inversion Accuracy on LR Images

We conducted water depth inversion on the original HSI from the HJ-2 A/B satellite, with the obtained water depth inversion maps shown in Figure 6. It can be seen that the RF model provides results closest to the true measured water depth map, followed by the MLP model. The SVR model performs the worst, showing significant depth errors, particularly around water boundaries. While the RF model effectively reflects overall water depth trends, jagged results are evident due to the resolution limitations of the original HSIs.

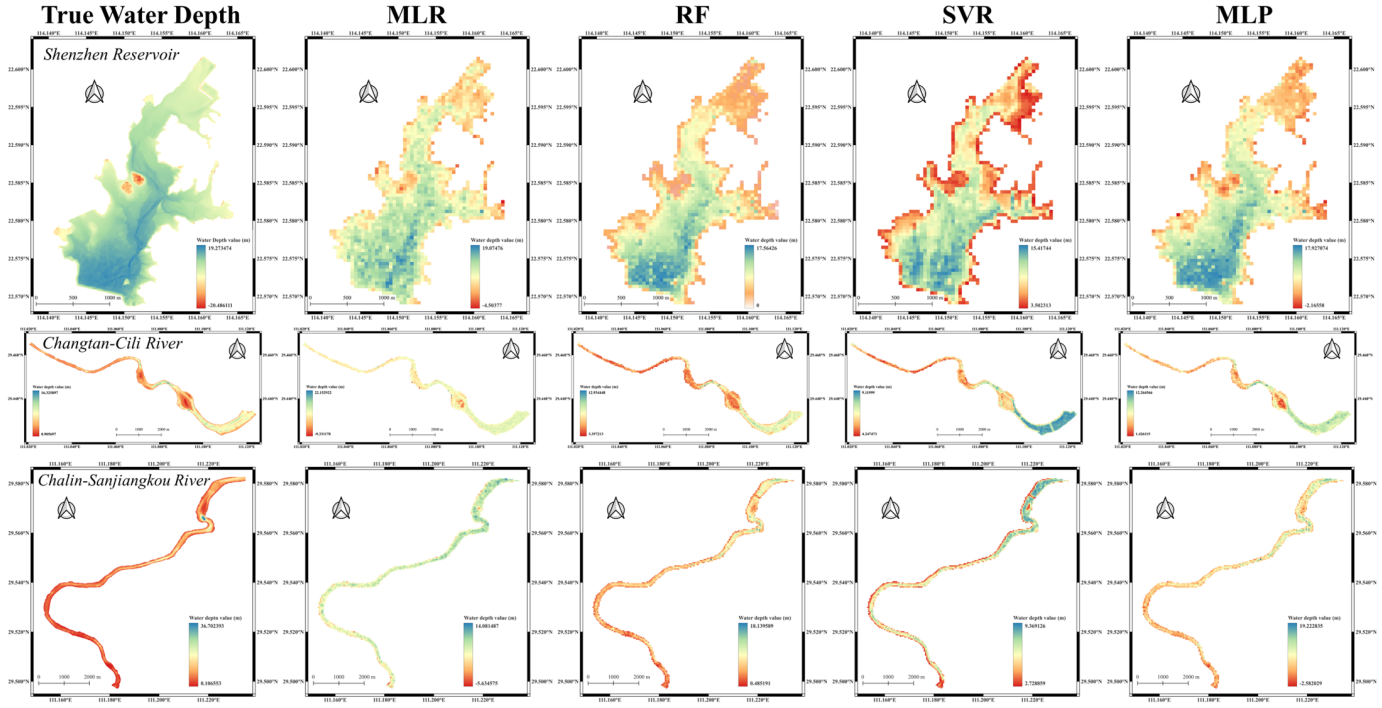


Figure 6. Water depth inversion results of original LR HJ2-A/B HSIs on three study areas.

We directly compared the accuracy of water depth inversion using the original LR HSIs. Table 2 presents the model validation accuracy for different water depth inversion models across study areas, with the best validation accuracy in each region highlighted in red. As shown in Table 2, the RF model has the best performance overall, with the highest metrics in both river areas and only slightly lower than MLP in the Shenzhen reservoir. Among the four water depth inversion models, the SVR shows lower validation accuracy compared to the RF and MLP models.

Table 2. Water depth inversion accuracy of original LR HSIs in three study areas.

Area	MLR		RF		SVR		MLP	
	MAE	MAPE	MAE	MAPE	MAE	MAPE	MAE	MAPE
Shenzhen Reservoir	2.025	33.285%	1.183	21.742%	2.286	44.217%	**1.156**	**19.280%**
Changtan-Cili River	1.120	15.715%	**0.761**	**10.647%**	1.154	15.598%	0.863	11.873%
Chalin-Sanjiangkou River	2.125	58.642%	**1.510**	**42.430%**	2.178	59.276%	1.752	46.640%

3.2.2. Water Depth Inversion Accuracy on SR Images

The HJ-2 A/B HSIs processed with SR were then used to repeat the water depth inversion steps. To visually compare water depth inversion results before and after SR, we present the water depth inversion maps of the Shenzhen reservoir area in Figure 7. As shown, compared to the original LR inversion maps, SR-processed results are more precise,

with significantly enhanced detail in water characterization. In addition, the overall water depth range and variation trend remain consistent before and after SR processing (see the second row in Figure 7), indicating that SR does not substantially alter water depth inversion results, thereby ensuring reliability. The consistency and differences among various water inversion models are preserved as well.

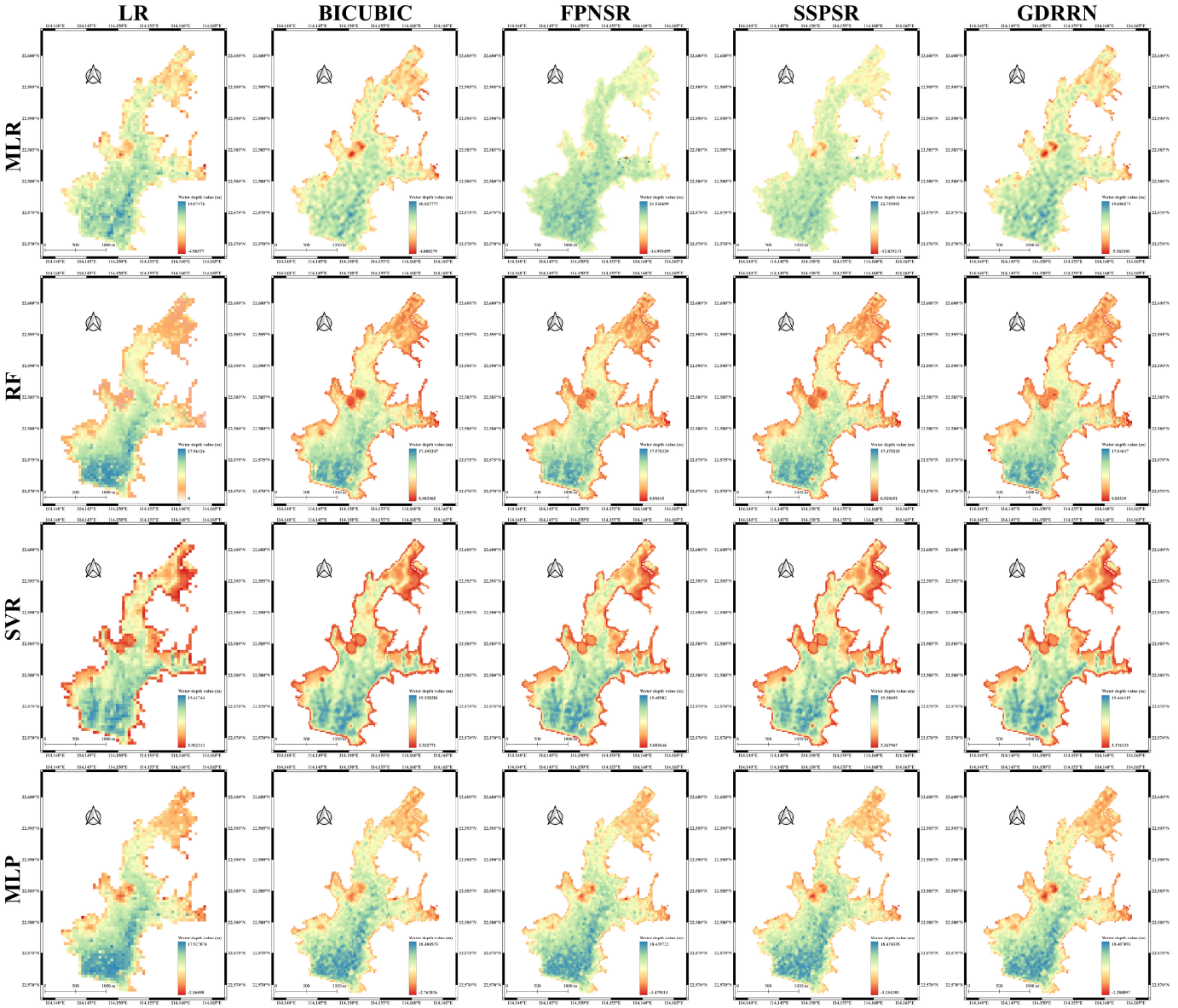


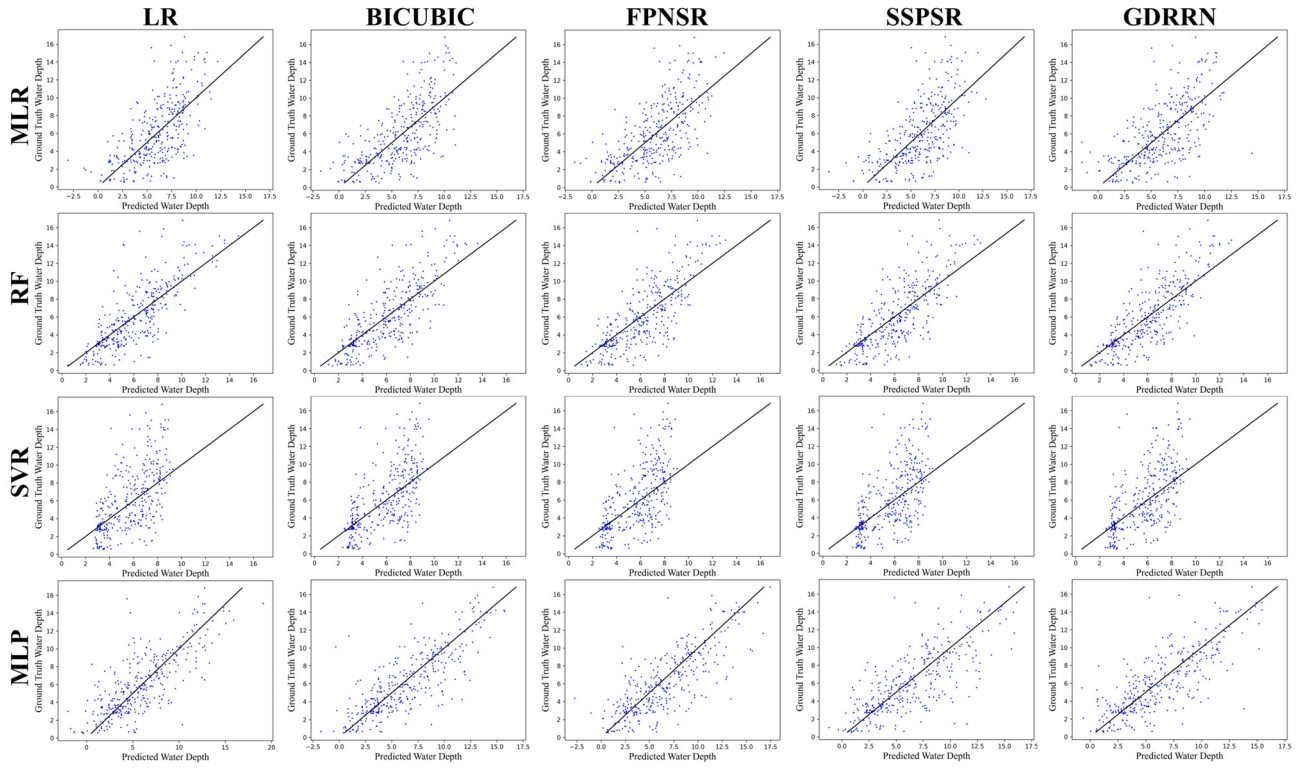
Figure 7. Water depth inversion results of super-resolved HJ2-A/B HSIs on Shenzhen reservoir area.

Using the same position and number of sample points, we reinverted water depth on images processed by different HSI SR models and evaluated the validation accuracy of test samples in Table 3, with the optimal accuracy of each study area highlighted in red. A comparative analysis of Tables 2 and 3 reveals that SR processing does not significantly degrade water depth inversion accuracy. In the Shenzhen Reservoir area, the MAE of the optimal MLP model increased by 0.136 m after SR, and MAPE rose by 2.908%. For the two river regions, the optimal RF model shows subtle accuracy loss. In the Chalin-Sanjiangkou River area, MAE and MAPE increased by 0.102 m and 3.454%, respectively. However, in the Changtan-Cili River region, MAE was reduced by 0.011 m. The results suggest that the SR technique can enhance the spatial resolution of the water depth inversion outcomes without compromising accuracy.

Table 3. Water depth inversion validation accuracy of super-resolved HSIs in three study areas.

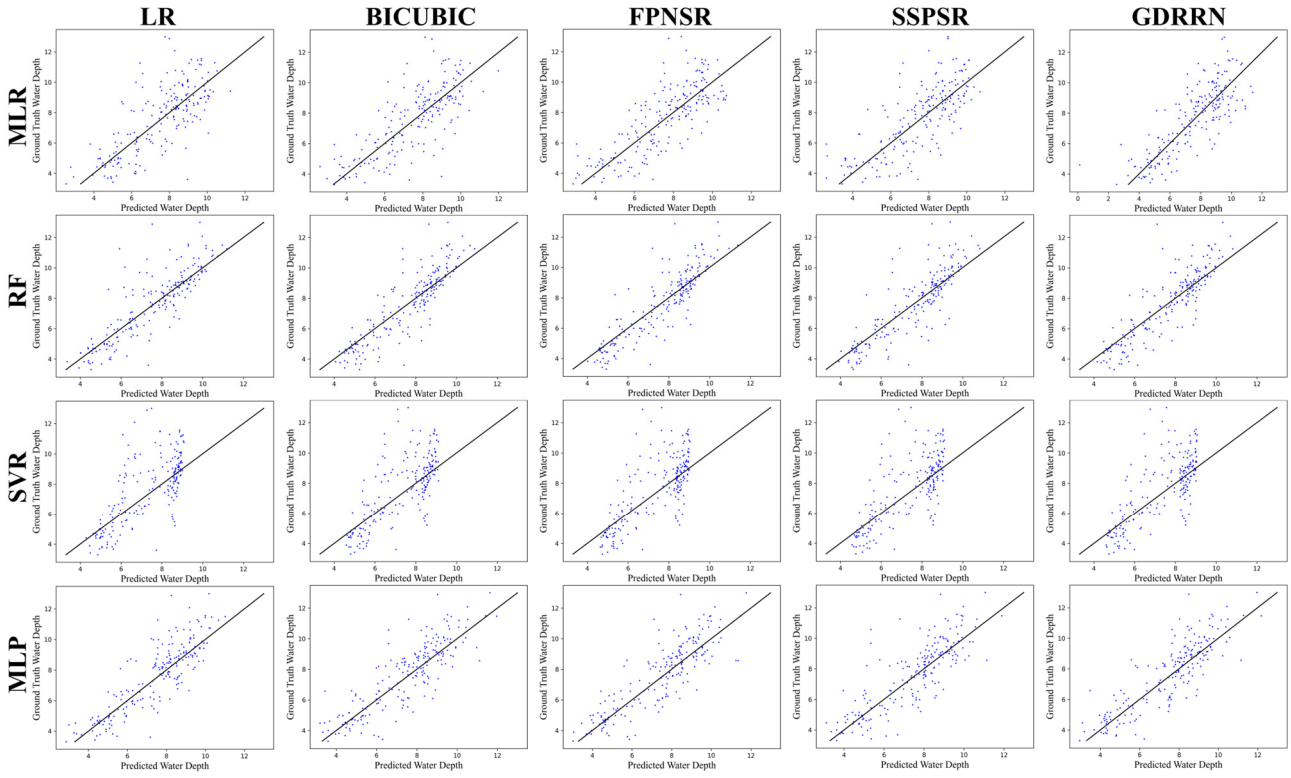
Area	SR Method	MLR		RF		SVR		MLP	
		MAE	MAPE	MAE	MAPE	MAE	MAPE	MAE	MAPE
Shenzhen Reservoir	BICUBIC	2.260	37.431%	1.498	27.054%	2.292	44.096%	1.377	23.590%
	FPNSR	2.216	36.481%	1.526	26.908%	2.329	43.804%	1.318	23.376%
	SSPSR	2.319	39.676%	1.546	26.809%	2.339	44.135%	1.370	23.148%
	GDRRN	2.329	38.463%	1.527	27.024%	2.270	42.576%	**1.292**	**22.188%**
Changtan-Cili River	BICUBIC	1.086	15.555%	0.794	11.644%	1.119	15.133%	0.907	12.770%
	FPNSR	1.113	15.693%	**0.750**	**10.806%**	1.104	14.944%	0.872	11.980%
	SSPSR	1.135	16.385%	0.794	11.416%	1.111	14.979%	0.935	12.998%
	GDRRN	1.058	14.72%	0.794	11.513%	1.097	14.805%	0.870	12.178%
Chalin-Sanjiangkou River	BICUBIC	2.106	54.593%	1.670	45.694%	2.007	54.622%	1.642	**40.540%**
	FPNSR	2.138	58.288%	1.697	49.266%	2.114	57.128%	1.785	47.574%
	SSPSR	2.206	62.008%	1.704	49.203%	2.112	57.046%	1.808	46.530%
	GDRRN	2.112	57.162%	**1.612**	45.884%	2.072	55.861%	1.682	44.285%

In Figure 8, we presented the scatter plots of the true values and the predicted values from different water depth inversion models applied to both LR and SR HSIs, providing a visual comparison of the accuracy across the water inversion models. As shown in Figure 8, across three different water bodies, the RF model exhibits a more concentrated distribution of scatter points, followed by the MLP model, indicating that these two models offer the best fitting accuracy for the water depth values and demonstrate better generalization across areas. The MLR and SVR models show a more discrete distribution of data points, suggesting weaker fitting ability. It is worth noting that the distribution of the SVR model in the Shenzhen Reservoir differs significantly from that in the two river areas, highlighting its relatively poor generalization ability across different water scenarios.

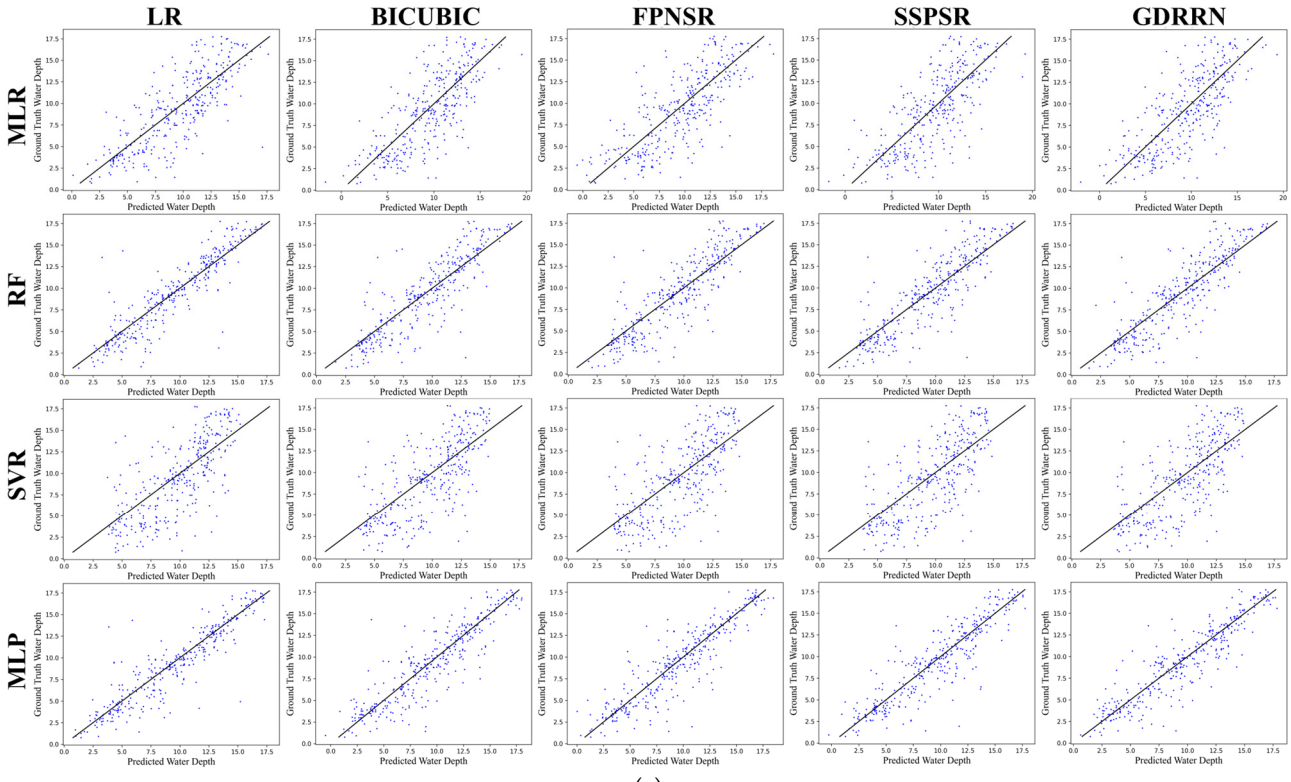


(**a**)

Figure 8. *Cont.*



(**b**)



(**c**)

Figure 8. Scatter plots of water depth inversion results with ground truth values based on super-resolved HSIs of different areas. (**a**) Chalin-Sanjiangkou River; (**b**) Changtan-Cili River; (**c**) Shenzhen reservoir.

To visually compare accuracy changes across the three water scenarios with different SR methods and water depth inversion models, we plotted the MAE and MAPE metrics in Figure 9. In the Changtan-Cili River, RF achieves the lowest MAE and MAPE values.

As for the MLP model, it performs well in the Shenzhen reservoir area, where it achieves the best MAE and MAPE, suggesting that MLP may be suitable for complex, nonlinear relationships. This result aligns with the water depth inversion outcomes for the original LR images in Table 2. Regarding the performance of SR models, traditional BICUBIC interpolation tends to perform worse across most metrics. By contrast, the FPNSR and GDRRN models generally show better performance across areas, underscoring their effectiveness in enhancing predictive capabilities for water depth inversion. For example, GDRRN achieves the lowest MAE in both river areas. Significant variations in the optimal metrics for each region suggest that each area has unique characteristics impacting water depth inversion accuracy. MLP appears particularly effective in more homogenous and stable scenes (like Shenzhen reservoir), while the RF model demonstrates robustness across multiple areas.

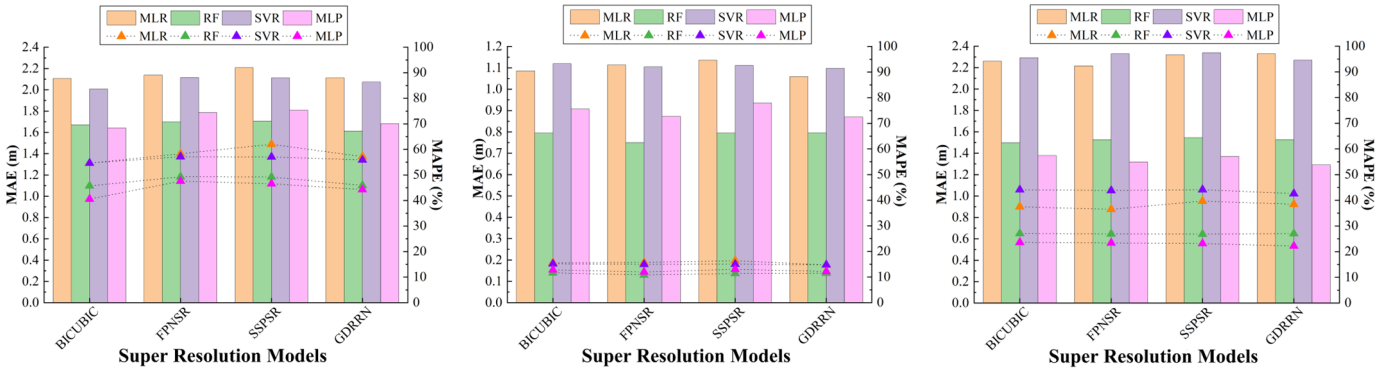


Figure 9. Water depth inversion accuracy based on super-resolved HSIs of different areas. (**a**) Chalin-Sanjiangkou River; (**b**) Changtan-Cili River; (**c**) Shenzhen reservoir.

4. Discussion

In this study, we only evaluated and discussed the accuracy of water depth inversion under the condition of ×2 HSI SR. Further research is needed to assess the effectiveness of SR processing at ×4 HSI SR or higher, as this study is limited by the current HSI SR dataset. For a more in-depth analysis of the HSI water depth inversion task, we further examined the following aspects: (1) the difference between the global region modeling and the sub-region modeling for each water depth inversion model; (2) the generalization ability of water depth models across different water bodies; and (3) the impact of radiometric preprocessing, specifically atmospheric correction, on HSI water depth inversion.

4.1. Water Depth Inversion of Whole-Region and Subregion Modeling

In the previous analysis, we primarily built and verified the water depth inversion models for each study area individually. To examine the differences between the whole-region modeling and the subregional modeling, we aggregated the sample points from the three study areas to perform a unified water depth inversion. The training and verification accuracy of the whole-region modeling is shown in Table 4, while Table 5 shows the verification accuracy of the whole-region water depth model within each study area.

Table 4. The training and validation accuracy of water depth inversion using super-resolved hyperspectral images from whole-region modeling.

SR Method	MLR		RF		SVR		MLP	
	MAE	MAPE	MAE	MAPE	MAE	MAPE	MAE	MAPE
BICUBIC	2.265	49.294%	1.443	31.650%	2.242	48.197%	1.576	32.947%
FPNSR	2.215	49.129%	1.440	32.517%	2.256	48.933%	1.572	33.299%
SSPSR	2.287	51.029%	1.478	33.463%	2.257	48.798%	1.588	33.234%
GDRRN	2.288	50.214%	1.440	32.689%	2.247	48.172%	1.525	32.289%

Table 5. Subregion validation accuracy of water depth inversion using super-resolved hyperspectral images from whole-region modeling.

Area	SR Method	MLR		RF		SVR		MLP	
		MAE	MAPE	MAE	MAPE	MAE	MAPE	MAE	MAPE
Shenzhen Reservoir	BICUBIC	2.504	43.289%	1.521	27.868%	2.709	50.953%	1.636	27.201%
	FPNSR	2.360	40.151%	1.546	27.431%	2.721	51.006%	1.650	26.769%
	SSPSR	2.510	43.918%	1.595	29.069%	2.741	51.427%	1.697	27.328%
	GDRRN	2.429	42.204%	1.525	27.819%	2.713	50.031%	1.623	26.639%
Changtan-Cili River	BICUBIC	1.586	23.607%	0.930	14.162%	1.303	18.606%	1.000	14.703%
	FPNSR	1.635	24.303%	0.823	12.161%	1.253	17.688%	0.985	13.857%
	SSPSR	1.644	24.284%	0.876	13.172%	1.259	17.594%	0.969	13.837%
	GDRRN	1.651	25.055%	0.894	13.542%	1.260	17.705%	0.907	12.727%
Chalin-Sanjiangkou River	BICUBIC	2.424	70.207%	1.664	45.585%	2.330	62.771%	1.833	48.373%
	FPNSR	2.410	72.479%	1.694	49.413%	2.380	64.559%	1.823	49.308%
	SSPSR	2.442	73.653%	1.713	49.636%	2.355	63.688%	1.814	48.809%
	GDRRN	2.520	72.802%	1.674	48.665%	2.358	63.461%	1.765	48.181%

As shown in Table 4, different SR methods have minimal influence on water depth inversion accuracy when using the sample points from all three regions. Across different SR methods, the variation in MAE metrics is less than 0.1 m, and the maximum difference in MAPE metrics is under 2%, indicating that the selection of SR model does not significantly impact the fitting ability for water depth inverting in whole-region modeling. For model performance, the RF model achieves the optimal accuracies across the water depth inversion models, with the lowest MAE and competitive MAPE among them.

Comparing Table 3 with Table 5, the RF model outperforms other water depth inversion models in all areas under the whole-regional inversion scenario, reaffirming its robustness in water depth inversion. In terms of the optimal inversion accuracy of each area, higher accuracy is achieved when using the sample points specific to each subregion. For example, in the Changtan-Cili River, based on the images processed by the FPNSR method, the RF water depth inversion model improves MAE by 0.073 m and MAPE by 1.355%. This is because water depth range, water quality, suspended solids, and the model performance vary between areas, making it undoubtedly more challenging to account for these factors within a single inversion model.

Furthermore, the differences in accuracy may become more pronounced when using multiple water depth inversion models. For instance, in the Shenzhen Reservoir area, using the GDRRN-processed images, the MLP model in subregion modeling yields MAE and MAPE of 1.623 m and 26.639%, while the RF model in whole-region modeling yields MAE and MAPE of 1.525 m and 27.819%. The differences between these metrics are not negligible. Therefore, the inversion models of the water bodies in different areas should be constructed individually when data samples are sufficient.

4.2. Analysis of Model Generalization Ability Across Different Water Bodies

To further assess the generalization ability of the water depth inversion models, we performed cross-validation across various water bodies, with the results presented in Table 6. By comparing Tables 3 and 6, we observe significant differences in the generalization of the water depth inversion models. Among them, the model of Shenzhen Reservoir shows the best generalization ability, while the model of Chalin-Sanjiangkou River exhibits the weakest generalization ability. For example, when the RF model trained on Shenzhen Reservoir was cross-validated in two river areas, the MAE and MAPE increased by up to 1.23 m and 32.745%, respectively. In contrast, when the RF model trained on the Chalin-Sanjiangkou River was cross-validated in the other two areas, the MAE and MAPE increased by up to 3.835 m and 12.602%, respectively. Among the four water depth models, the RF model shows the best overall performance and generalization ability, while the MLR

model has the worst generalization ability, suggesting that a simple linear model is less suitable for water depth inversion in multiclass scenarios.

Table 6. Water depth inversion validation accuracy across three study areas.

Train Area	Validation Area	SR Method	MLR		RF		SVR		MLP	
			MAE	MAPE	MAE	MAPE	MAE	MAPE	MAE	MAPE
Shenzhen Reservoir	Changtan-Cili River	BICUBIC	3.242	43.340%	**1.786**	**22.451%**	2.473	43.593%	2.945	40.613%
		FPNSR	4.584	58.096%	**1.760**	**21.494%**	2.644	46.922%	2.094	32.722%
		SSPSR	3.367	43.272%	**1.951**	**23.547%**	2.764	48.430%	2.051	32.802%
		GDRRN	3.065	41.789%	**1.968**	**24.101%**	2.757	48.582%	2.549	35.126%
	Chalin-Sanjiangkou River	BICUBIC	3.657	138.167%	2.669	**59.799%**	**2.428**	74.390%	2.714	75.997%
		FPNSR	3.930	98.381%	**2.536**	**59.122%**	2.552	82.217%	2.816	95.575%
		SSPSR	3.713	89.299%	**2.532**	**59.004%**	2.541	80.824%	2.808	91.135%
		GDRRN	3.065	100.479%	2.729	**56.443%**	**2.495**	77.616%	2.750	88.803%
Changtan-Cili River	Shenzhen Reservoir	BICUBIC	5.619	57.354%	3.848	**56.565%**	**3.433**	60.552%	3.804	66.455%
		FPNSR	4.136	**53.916%**	3.758	54.552%	**3.396**	59.516%	3.464	66.529%
		SSPSR	3.946	**52.013%**	3.904	56.093%	**3.403**	59.780%	3.595	65.306%
		GDRRN	5.698	58.820%	3.884	**54.940%**	**3.401**	60.282%	3.528	68.172%
	Chalin-Sanjiangkou River	BICUBIC	6.441	148.446%	2.757	65.214%	2.652	64.530%	**2.340**	**59.979%**
		FPNSR	5.991	126.948%	2.617	68.155%	2.639	66.424%	**2.409**	**61.363%**
		SSPSR	3.304	68.676%	2.719	63.944%	2.668	65.572%	**2.494**	**61.253%**
		GDRRN	5.910	110.700%	2.734	71.710%	**2.698**	65.936%	2.758	**59.611%**
Chalin-Sanjiangkou River	Shenzhen Reservoir	BICUBIC	10.218	183.020%	5.505	58.296%	**4.188**	**51.218%**	4.781	53.924%
		FPNSR	8.576	160.723%	4.777	55.751%	**4.280**	**51.601%**	4.280	52.231%
		SSPSR	10.714	194.674%	5.259	57.151%	4.231	51.887%	**3.726**	**50.437%**
		GDRRN	13.813	243.514%	5.186	55.763%	**4.204**	**51.786%**	4.607	54.670%
	Changtan-Cili River	BICUBIC	29.325	409.343%	**2.181**	**31.880%**	2.438	38.295%	2.839	42.642%
		FPNSR	19.963	270.603%	**1.720**	**25.203%**	2.036	32.075%	2.907	42.659%
		SSPSR	17.807	248.639%	**1.898**	**27.085%**	2.071	32.293%	2.151	32.936%
		GDRRN	27.631	378.699%	**2.129**	**30.489%**	2.371	37.342%	3.150	45.149%

Additionally, it is evident that the accuracy of the two river regions is close during the cross-validation. Taking the RF model as an example, the MAE was consistently around 2 m (ranging from 1.720 m to 2.757 m) when the water depth models of the river area were mutually validated. The accuracy of MAE ranged from 1.760 m to 5.505 m during the cross-validation between reservoir and river areas, indicating that different types of water bodies should be independently modeled when constructing water depth inversion models. This is still because the water quality and depth of water in reservoirs and rivers are quite different, as we have mentioned before.

4.3. Water Depth Inversion on DN Values

In the previous experiments, we used the reflectance value obtained after atmospheric correction for water depth inversion. However, due to the diversity and varying accuracy of atmospheric correction methods, selecting an appropriate atmospheric correction model for practical application remains a challenge. Moreover, in most scenarios, the HSIs provided by satellite image vendors have not undergone absolute radiometric calibration and atmospheric correction, and their pixel values are the original DNs. To address this, we conducted an additional experiment of water depth inversion directly on the Level-1 (DN value) HSIs, with the obtained water depth inversion accuracy presented in Table 7.

By comparing Tables 3 and 7, it is clear that the accuracy of water depth inversion using reflectance and DN is quite similar, and the water depth inversion accuracy using DN values is even slightly better than that using reflectance values in some cases. For instance, in the Changtan-Cili River and Chalin-Sanjiangkou River areas, the RF water depth inversion model using DN values yields slightly better accuracy metrics than when

using reflectance values, especially when applied to FPNSR-processed HSIs. This suggests that preprocessing steps, such as atmospheric correction, are not indispensable for water depth inversion from HSIs.

Table 7. Accuracy of water depth inversion on DN values using super-resolved HSIs.

Area	SR Method	MLR		RF		SVR		MLP	
		MAE	MAPE	MAE	MAPE	MAE	MAPE	MAE	MAPE
Shenzhen Reservoir	BICUBIC	2.282	37.620%	1.495	26.939%	2.294	44.117%	1.351	22.784%
	FPNSR	2.179	35.839%	1.534	27.012%	2.323	43.693%	1.364	24.086%
	SSPSR	2.308	39.209%	1.549	26.759%	2.337	43.997%	1.327	22.823%
	GDRRN	2.352	38.826%	1.515	26.781%	2.270	42.559%	**1.321**	**22.677%**
Changtan-Cili River	BICUBIC	1.109	15.598%	0.800	11.746%	1.115	15.080%	0.911	12.751%
	FPNSR	1.137	16.021%	**0.747**	**10.766%**	1.103	14.930%	0.878	12.124%
	SSPSR	1.123	16.411%	0.790	11.328%	1.112	14.982%	0.916	12.782%
	GDRRN	0.996	13.690%	0.796	11.561%	1.095	14.755%	0.880	12.262%
Chalin-Sanjiangkou River	BICUBIC	2.103	54.873%	1.619	45.343%	2.065	56.215%	1.812	46.408%
	FPNSR	2.121	57.323%	1.694	49.131%	2.112	57.153%	1.763	47.618%
	SSPSR	2.329	64.917%	1.855	50.949%	2.083	57.769%	1.984	50.033%
	GDRRN	2.102	56.165%	**1.615**	45.721%	2.076	55.928%	1.696	**43.875%**

As discussed above, the accuracy of water depth inversion is influenced by several complex factors, including the SR algorithm, inversion algorithm, water quality, and tidal effects. Water quality factors, such as suspended matter and sediment content, should be considered in water depth inversion, particularly for water bodies in diverse environmental conditions. However, due to the lack of measured water quality data to support quantitative analysis, we plan to collect water quality data to assist the follow-up research. Additionally, our study primarily focuses on inland water bodies, and the tidal effects should be taken into account to further improve the accuracy of water depth measurements. Given the limitations of the imaging time of HJ2-A/B satellite HSIs, our study does not analyze the impact of tides on water depth inversion, but this will be investigated in future research.

5. Conclusions

In this study, we validated the potential of HSI for estimating water depth in various water bodies utilizing DL-based SR technology. The results revealed several key findings: (1) SR effectively enhances the spatial resolution of HSI from 48 m to 24 m, maintaining a high PNSR over 37.0, an SSIM exceeding 0.92, and a SAM of below 2.50; (2) the optimal retrieval algorithms vary by water bodies, with RF being preferred for river depth inversion and MLP for water reservoirs; (3) the integration of SR technology with the optimal water depth inversion model achieves higher resolution results with accuracy comparable to LR HSIs, with MAE under 0.150 m and MAPE below 3.50%; (4) atmospheric correction is not a critical preprocessing step for water depth inversion. Future research should focus on the impact of water quality and tidal conditions on water depth parameters, providing both quantitative and qualitative explanations for variations in inversion accuracy. This study represents a novel strategy for remotely sensed water depth across water bodies with high spatial resolution, advancing the field of environmental management.

Author Contributions: Conceptualization, S.Z. and M.L.; methodology, S.Z. and X.W.; software, B.Z. and X.C.; validation, K.H. and C.G.; formal analysis, B.Z. and J.X.; investigation, S.Z. and K.H.; resources, K.H. and B.Z.; data curation, B.Z. and J.X.; writing—original draft preparation, S.Z. and X.W.; writing—review and editing, S.Z. and X.W.; visualization, S.Z. and X.W.; supervision, X.C.; project administration, S.Z.; funding acquisition, S.Z. All authors have read and agreed to the published version of the manuscript.

Funding: This research was supported by a grant from the Key Laboratory of Emergency Satellite Engineering and Application, Ministry of Emergency Management (No. CKSD20231247/KJ), and National Key Research and Development Program of China (2023YFC3209502).

Data Availability Statement: The raw data supporting the conclusions of this article will be made available by the authors on request.

Acknowledgments: The authors are grateful to the Key Laboratory of Emergency Satellite Engineering and Application, Ministry of Emergency Management, and China Resources Satellite Application Center for providing valuable satellite image data to support this paper and experiment. The authors would like to thank the anonymous reviewers for their valuable comments and suggestions.

Conflicts of Interest: The authors declare no conflicts of interest.

References

1. Kutser, T.; Hedley, J.; Giardino, C.; Roelfsema, C.; Brando, V.E. Remote Sensing of Shallow Waters–A 50 Year Retrospective and Future Directions. *Remote Sens. Environ.* **2020**, *240*, 111619. [CrossRef]
2. Setiawan, K.T.; Suwargana, N.; Ginting, D.N.B.; Manessa, M.D.M.; Anggraini, N.; Adawiah, S.W.; Julzarika, A.; Surahman, S.; Rosid, S.; Supardjo, A.H. Bathymetry Extraction from SPOT 7 Satellite Imagery Using Random Forest Methods. *Int. J. Remote Sens. Earth Sci.* **2019**, *16*, 23–30. [CrossRef]
3. Ashphaq, M.; Srivastava, P.K.; Mitra, D. Review of Near-Shore Satellite Derived Bathymetry: Classification and Account of Five Decades of Coastal Bathymetry Research. *J. Ocean Eng. Sci.* **2021**, *6*, 340–359. [CrossRef]
4. Bergsma, E.W.J.; Almar, R.; Rolland, A.; Binet, R.; Brodie, K.L.; Bak, A.S. Coastal Morphology from Space: A Showcase of Monitoring the Topography-Bathymetry Continuum. *Remote Sens. Environ.* **2021**, *261*, 112469. [CrossRef]
5. Chen, B.; Krajewski, W.F.; Goska, R.; Young, N. Using LiDAR Surveys to Document Floods: A Case Study of the 2008 Iowa Flood. *J. Hydrol.* **2017**, *553*, 338–349. [CrossRef]
6. Albright Blomberg, A.E.; Austeng, A.; Hansen, R.E.; Synnes, S.A.V. Improving Sonar Performance in Shallow Water Using Adaptive Beamforming. *IEEE J. Ocean. Eng.* **2013**, *38*, 297–307. [CrossRef]
7. Cesbron, G.; Melet, A.; Almar, R.; Lifermann, A.; Tullot, D.; Crosnier, L. Pan-European Satellite-Derived Coastal Bathymetry—Review, User Needs and Future Services. *Front. Mar. Sci.* **2021**, *8*, 740830. [CrossRef]
8. Caballero, I.; Stumpf, R.P. Retrieval of Nearshore Bathymetry from Sentinel-2A and 2B Satellites in South Florida Coastal Waters. *Estuar. Coast. Shelf Sci.* **2019**, *226*, 106277. [CrossRef]
9. Nan, Y.; Jianhui, L.; Wenbo, M.; Wangjun, L.; Di, W.; Wanchao, G.; Changhao, S. Water Depth Retrieval Models of East Dongting Lake, China, Using GF-1 Multi-Spectral Remote Sensing Images. *Glob. Ecol. Conserv.* **2020**, *22*, e01004. [CrossRef]
10. Xu, Y.; Cao, B.; Deng, R.; Cao, B.; Liu, H.; Li, J. Bathymetry over Broad Geographic Areas Using Optical High-Spatial-Resolution Satellite Remote Sensing without in-Situ Data. *Int. J. Appl. Earth Obs. Geoinf.* **2023**, *119*, 103308. [CrossRef]
11. Majozi, N.P.; Salama, M.S.; Bernard, S.; Harper, D.M.; Habte, M.G. Remote Sensing of Euphotic Depth in Shallow Tropical Inland Waters of Lake Naivasha Using MERIS Data. *Remote Sens. Environ.* **2014**, *148*, 178–189. [CrossRef]
12. Legleiter, C.J.; Roberts, D.A. A Forward Image Model for Passive Optical Remote Sensing of River Bathymetry. *Remote Sens. Environ.* **2009**, *113*, 1025–1045. [CrossRef]
13. Amini, L.; Kakroodi, A.A. Bathymetry Monitoring of Shallow Coastal Environment Using Remote Sensing Data. *Remote Sens. Appl. Soc. Environ.* **2024**, *36*, 101255. [CrossRef]
14. Cracknell, A.P.; Ibrahim, M. Bathymetry Studies on the Coastal Waters (Red Sea) of Jeddah, Saudi Arabia, Using Shuttle MOMS-01 Data. *Int. J. Remote Sens.* **1988**, *9*, 1161–1165. [CrossRef]
15. Roy, S.; Das, B.S. Estimation of Euphotic Zone Depth in Shallow Inland Water Using Inherent Optical Properties and Multispectral Remote Sensing Imagery. *J. Hydrol.* **2022**, *612*, 128293. [CrossRef]
16. Shang, S.; Lee, Z.; Wei, G. Characterization of MODIS-Derived Euphotic Zone Depth: Results for the China Sea. *Remote Sens. Environ.* **2011**, *115*, 180–186. [CrossRef]
17. Pushparaj, J.; Hegde, A.V. Estimation of Bathymetry along the Coast of Mangaluru Using Landsat-8 Imagery. *Int. J. Ocean Clim. Syst.* **2017**, *8*, 71–83. [CrossRef]
18. Simon, A.; Shanmugam, P. Estimation of the Spectral Diffuse Attenuation Coefficient of Downwelling Irradiance in Inland and Coastal Waters from Hyperspectral Remote Sensing Data: Validation with Experimental Data. *Int. J. Appl. Earth Obs. Geoinf.* **2016**, *49*, 117–125. [CrossRef]
19. Jalil, A.; Li, Y.; Zhang, K.; Gao, X.; Wang, W.; Khan, H.O.S.; Pan, B.; Ali, S.; Acharya, K. Wind-Induced Hydrodynamic Changes Impact on Sediment Resuspension for Large, Shallow Lake Taihu, China. *Int. J. Sediment Res.* **2019**, *34*, 205–215. [CrossRef]
20. Zhou, Q.; Zhang, Y.; Li, K.; Huang, L.; Yang, F.; Zhou, Y.; Chang, J. Seasonal and Spatial Distributions of Euphotic Zone and Long-Term Variations in Water Transparency in a Clear Oligotrophic Lake Fuxian, China. *J. Environ. Sci.* **2018**, *72*, 185–197. [CrossRef]
21. He, J.; Zhang, S.; Cui, X.; Feng, W. Remote Sensing for Shallow Bathymetry: A Systematic Review. *Earth-Sci. Rev.* **2024**, *258*, 104957. [CrossRef]

22. Zeng, F.; Song, C.; Cao, Z.; Xue, K.; Lu, S.; Chen, T.; Liu, K. Monitoring Inland Water via Sentinel Satellite Constellation: A Review and Perspective. *ISPRS J. Photogramm. Remote Sens.* **2023**, *204*, 340–361. [CrossRef]
23. Jay, S.; Guillaume, M. A Novel Maximum Likelihood Based Method for Mapping Depth and Water Quality from Hyperspectral Remote-Sensing Data. *Remote Sens. Environ.* **2014**, *147*, 121–132. [CrossRef]
24. Li, Z.; Leong, W.J.; Durand, M.; Howat, I.; Wadkowski, K.; Yadav, B.; Moortgat, J. Super-Resolution Deep Neural Networks for Water Classification from Free Multispectral Satellite Imagery. *J. Hydrol.* **2023**, *626*, 130248. [CrossRef]
25. Jiang, J.; Sun, H.; Liu, X.; Ma, J. Learning Spatial-Spectral Prior for Super-Resolution of Hyperspectral Imagery. *IEEE Trans. Comput. Imaging* **2020**, *6*, 1082–1096. [CrossRef]
26. Wang, X.; Hu, Q.; Jiang, J.; Ma, J. A Group-Based Embedding Learning and Integration Network for Hyperspectral Image Super-Resolution. *IEEE Trans. Geosci. Remote Sens.* **2022**, *60*, 5541416. [CrossRef]
27. Wang, X.; Ma, J.; Jiang, J. Hyperspectral Image Super-Resolution via Recurrent Feedback Embedding and Spatial–Spectral Consistency Regularization. *IEEE Trans. Geosci. Remote Sens.* **2022**, *60*, 5503113. [CrossRef]
28. Dong, W.; Zhou, C.; Wu, F.; Wu, J.; Shi, G.; Li, X. Model-Guided Deep Hyperspectral Image Super-Resolution. *IEEE Trans. Image Process.* **2021**, *30*, 5754–5768. [CrossRef]
29. Lu, H.; Qiao, D.; Li, Y.; Wu, S.; Deng, L. Fusion of China ZY-1 02D Hyperspectral Data and Multispectral Data: Which Methods Should Be Used? *Remote Sens.* **2021**, *13*, 2354. [CrossRef]
30. Li, K.; Zhang, W.; Yu, D.; Tian, X. HyperNet: A Deep Network for Hyperspectral, Multispectral, and Panchromatic Image Fusion. *ISPRS J. Photogramm. Remote Sens.* **2022**, *188*, 30–44. [CrossRef]
31. Wang, X.; Wang, X.; Song, R.; Zhao, X.; Zhao, K. MCT-Net: Multi-Hierarchical Cross Transformer for Hyperspectral and Multispectral Image Fusion. *Knowl. Based Syst.* **2023**, *264*, 110362. [CrossRef]
32. Vivone, G. Multispectral and Hyperspectral Image Fusion in Remote Sensing: A Survey. *Inf. Fusion* **2023**, *89*, 405–417. [CrossRef]
33. Li, J.; Li, Y.; Yu, Y.; Li, J.; Cai, X.; Lyu, L.; Wang, H.; Dong, X.; Song, M.; Zhu, Y.; et al. Evaluating the Capabilities of China's New Satellite HJ-2 for Monitoring Chlorophyll a Concentration in Eutrophic Lakes. *Int. J. Appl. Earth Obs. Geoinf.* **2024**, *126*, 103618. [CrossRef]
34. Dong, C.; Loy, C.C.; He, K.; Tang, X. Learning a Deep Convolutional Network for Image Super-Resolution. In Proceedings of the Computer Vision–ECCV 2014, Zurich, Switzerland, 6–12 September 2014; Fleet, D., Pajdla, T., Schiele, B., Tuytelaars, T., Eds.; Springer International Publishing: Cham, Switzerland, 2014; Volume 8692, pp. 184–199.
35. Goodfellow, I.; Pouget-Abadie, J.; Mirza, M.; Xu, B.; Warde-Farley, D.; Ozair, S.; Courville, A.; Bengio, Y. Generative Adversarial Nets. In Proceedings of the Advances in Neural Information Processing Systems 27 (NIPS 2014), Cambridge, MA, USA, 8–13 December 2014; Volume 2, pp. 2672–2680.
36. Ledig, C.; Theis, L.; Huszar, F.; Caballero, J.; Cunningham, A.; Acosta, A.; Aitken, A.; Tejani, A.; Totz, J.; Wang, Z.; et al. Photo-Realistic Single Image Super-Resolution Using a Generative Adversarial Network. In Proceedings of the 2017 IEEE Conference on Computer Vision and Pattern Recognition (CVPR), Honolulu, HI, USA, 21–26 July 2017; pp. 105–114.
37. Lim, B.; Son, S.; Kim, H.; Nah, S.; Lee, K.M. Enhanced Deep Residual Networks for Single Image Super-Resolution. In Proceedings of the 2017 IEEE Conference on Computer Vision and Pattern Recognition Workshops (CVPRW), Honolulu, HI, USA, 21–26 July 2017; pp. 1132–1140.
38. Wang, X.; Yu, K.; Wu, S.; Gu, J.; Liu, Y.; Dong, C.; Qiao, Y.; Loy, C.C. ESRGAN: Enhanced Super-Resolution Generative Adversarial Networks. In Proceedings of the Computer Vision–ECCV 2018 Workshops, Munich, Germany, 8–14 September 2018; Leal-Taixé, L., Roth, S., Eds.; Springer International Publishing: Cham, Switzerland, 2019; Volume 11133, pp. 63–79.
39. Zhang, Y.; Li, K.; Li, K.; Wang, L.; Zhong, B.; Fu, Y. Image Super-Resolution Using Very Deep Residual Channel Attention Networks. In *Proceedings of the Computer Vision–ECCV 2018*; Springer International Publishing: Cham, Switzerland, 2018.
40. Zhao, H.; Kong, X.; He, J.; Qiao, Y.; Dong, C. Efficient Image Super-Resolution Using Pixel Attention. In Proceedings of the Computer Vision–ECCV 2020 Workshops, Glasgow, UK, 23–28 August 2020; Bartoli, A., Fusiello, A., Eds.; Springer International Publishing: Cham, Switzerland, 2020; Vol. 12537, pp. 56–72.
41. Chen, H.; Gu, J.; Zhang, Z. Attention in Attention Network for Image Super-Resolution. *arXiv* **2021**, arXiv:2104.09497.
42. Hui, Z.; Wang, X.; Gao, X. Fast and Accurate Single Image Super-Resolution via Information Distillation Network. In Proceedings of the 2018 IEEE/CVF Conference on Computer Vision and Pattern Recognition, Salt Lake City, UT, USA, 18–22 June 2018; pp. 723–731.
43. Hui, Z.; Gao, X.; Yang, Y.; Wang, X. Lightweight Image Super-Resolution with Information Multi-Distillation Network. In Proceedings of the 27th ACM International Conference on Multimedia, Nice, France, 15 October 2019; pp. 2024–2032.
44. Liu, J.; Tang, J.; Wu, G. Residual Feature Distillation Network for Lightweight Image Super-Resolution. In Proceedings of the Computer Vision–ECCV 2020 Workshops, Glasgow, UK, 23–28 August 2020; Bartoli, A., Fusiello, A., Eds.; Springer International Publishing: Cham, Switzerland, 2020; Volume 12537, pp. 41–55.
45. Li, X.; Zhang, L.; You, J. Domain Transfer Learning for Hyperspectral Image Super-Resolution. *Remote Sens.* **2019**, *11*, 694. [CrossRef]
46. Sun, S.; Bao, W.; Qu, K.; Feng, W.; Zhang, X.; Ma, X. Hyperspectral Image Super-Resolution Algorithm Based on Graph Regular Tensor Ring Decomposition. *Remote Sens.* **2023**, *15*, 4983. [CrossRef]
47. Qu, Y.; Qi, H.; Kwan, C.; Yokoya, N.; Chanussot, J. Unsupervised and Unregistered Hyperspectral Image Super-Resolution with Mutual Dirichlet-Net. *IEEE Trans. Geosci. Remote Sens.* **2022**, *60*, 5507018. [CrossRef]

48. Li, Y.; Zhang, L.; Dingl, C.; Wei, W.; Zhang, Y. Single Hyperspectral Image Super-Resolution with Grouped Deep Recursive Residual Network. In Proceedings of the 2018 IEEE Fourth International Conference on Multimedia Big Data (BigMM), Xi'an, China, 13–16 September 2018; pp. 1–4.
49. Sun, H.; Zhong, Z.; Zhai, D.; Liu, X.; Jiang, J. Hyperspectral Image Super-Resolution Using Multi-Scale Feature Pyramid Network. In Proceedings of the Digital TV and Wireless Multimedia Communication, Shanghai, China, 19–20 September 2019; Zhai, G., Zhou, J., Yang, H., An, P., Yang, X., Eds.; Springer: Singapore, 2020; Volume 1181, pp. 49–61.
50. Li, J.; Cui, R.; Li, B.; Song, R.; Li, Y.; Dai, Y.; Du, Q. Hyperspectral Image Super-Resolution by Band Attention Through Adversarial Learning. *IEEE Trans. Geosci. Remote Sens.* **2020**, *58*, 4304–4318. [CrossRef]
51. Paszke, A.; Gross, S.; Massa, F.; Lerer, A.; Bradbury, J.; Chanan, G.; Killeen, T.; Lin, Z.; Gimelshein, N.; Antiga, L.; et al. PyTorch: An Imperative Style, High-Performance Deep Learning Library. In *Proceedings of the 33rd International Conference on Neural Information Processing Systems*; Curran Associates Inc.: Red Hook, NY, USA, 2019; Volume 721, pp. 8026–8037.
52. Kingma, D.P.; Ba, J.L. Adam: A Method for Stochastic Optimization. In Proceedings of the 3rd International Conference on Learning Representations, San Diego, CA, USA, 7–9 May 2015; Volume 5.
53. Fraser, C.S.; Hanley, H.B. Bias Compensation in Rational Functions for Ikonos Satellite Imagery. *Photogramm. Eng. Remote Sens.* **2003**, *69*, 53–57. [CrossRef]
54. Fraser, C.S.; Hanley, H.B. Bias-Compensated RPCs for Sensor Orientation of High-Resolution Satellite Imagery. *Photogramm. Eng. Remote Sens.* **2005**, *71*, 909–915. [CrossRef]
55. Knudby, A.; Richardson, G. Incorporation of Neighborhood Information Improves Performance of SDB Models. *Remote Sens. Appl. Soc. Environ.* **2023**, *32*, 101033. [CrossRef]
56. Wei, S.; Qian, J.; Yali, R.; Ran, M. Comparative Study of Different Machine Learning Models for Remote Sensing Bathymetry Inversion. In Proceedings of the Intelligent and Fuzzy Techniques: Smart and Innovative Solutions, Istanbul, Turkey, 21–23 July 2020; Springer International Publishing: Cham, Switzerland, 2021; Volume 1197, pp. 1140–1148.
57. Moran, N.; Stringer, B.; Lin, B.; Hoque, M.T. Machine Learning Model Selection for Predicting Bathymetry. *Deep Sea Res. Part Oceanogr. Res. Pap.* **2022**, *185*, 103788. [CrossRef]
58. Zhou, W.; Tang, Y.; Jing, W.; Li, Y.; Yang, J.; Deng, Y.; Zhang, Y. A Comparison of Machine Learning and Empirical Approaches for Deriving Bathymetry from Multispectral Imagery. *Remote Sens.* **2023**, *15*, 393. [CrossRef]
59. Zhao, X.; Wang, D.; Xu, H.; Shi, Y.; Deng, Z.; Ding, Z.; Liu, Z.; Xu, X.; Lu, Z.; Wang, G.; et al. Water Deep Mapping from HJ-1B Satellite Data by a Deep Network Model in the Sea Area of Pearl River Estuary, China. *Open Geosci.* **2021**, *13*, 782–795. [CrossRef]
60. Mandlburger, G.; Kölle, M.; Nübel, H.; Soergel, U. BathyNet: A Deep Neural Network for Water Depth Mapping from Multispectral Aerial Images. *PFG J. Photogramm. Remote Sens. Geoinf. Sci.* **2021**, *89*, 71–89. [CrossRef]
61. Shen, W.; Chen, M.; Wu, Z.; Wang, J. Shallow-Water Bathymetry Retrieval Based on an Improved Deep Learning Method Using GF-6 Multispectral Imagery in Nanshan Port Waters. *IEEE J. Sel. Top. Appl. Earth Obs. Remote Sens.* **2023**, *16*, 8550–8562. [CrossRef]
62. Liu, X.; Song, Y.; Shen, C. Bathymetry Inversion Using a Deep-Learning-Based Surrogate for Shallow Water Equations Solvers. *Water Resour. Res.* **2024**, *60*, e2023WR035890. [CrossRef]
63. Kruse, F.A.; Lefkoff, A.B.; Boardman, J.W.; Heidebrecht, K.B.; Shapiro, A.T.; Barloon, P.J.; Goetz, A.F.H. Goetz the Spectral Image Processing System (SIPS)—Interactive Visualization and Analysis of Imaging Spectrometer Data. *Remote Sens. Environ.* **1993**, *44*, 192–201. [CrossRef]

Disclaimer/Publisher's Note: The statements, opinions and data contained in all publications are solely those of the individual author(s) and contributor(s) and not of MDPI and/or the editor(s). MDPI and/or the editor(s) disclaim responsibility for any injury to people or property resulting from any ideas, methods, instructions or products referred to in the content.